RSC Advances

PAPER

View Article Online
View Journal | View Issue

Cite this: *RSC Adv.*, 2026, **16**, 11648

Ligand-effect regulated selective catalytic oxidation of 2-chloroethyl ethyl sulfide in aqueous phase by Keplerate-type molybdenum-oxygen cluster {Mo_{132}}

Jianbo Yin,[ab] Liming Sun,[a] Yunshan Zhou *[a] and Lijuan Zhang*[a]

Received 23rd January 2026
Accepted 22nd February 2026

DOI: 10.1039/d6ra00608f

rsc.li/rsc-advances

Keplerate-type nano-polyoxometalates {Mo_{132}-Ac^-} and {Mo_{132}-SO_4^{2-}} were respectively used as catalysts, and H_2O_2 as the oxidant, for the catalytic oxidation of 2-chloroethyl ethyl sulfide (CEES), a simulant of mustard gas, in an aqueous solution. The decontamination conditions were optimized *via* the single-factor method. Under the optimized conditions, the CEES conversion rates catalyzed by {Mo_{132}-Ac^-} and {Mo_{132}-SO_4^{2-}} were 98.59% and 99.69%, respectively. After 5 cycles of reuse, both catalysts maintained a CEES conversion rate of over 90% and a selectivity of over 99%. The catalytic decontamination processes of CEES by {Mo_{132}-Ac^-} and {Mo_{132}-SO_4^{2-}} both followed first-order reaction kinetics, with kinetic constants of 0.39 min^{-1} and 0.60 min^{-1}, respectively. Compared with {Mo_{132}-Ac^-}, {Mo_{132}-SO_4^{2-}} with more negative charges exhibited higher catalytic activity, showing a significant ligand effect. By adjusting the amount of the catalyst and H_2O_2, CEES can be selectively catalytically oxidized to low-toxicity 2-chloroethyl ethyl sulfoxide (CEESO).

1 Introduction

Mustard gas (HD) is an infamous chemical warfare agent. The decontamination of HD and its simulant 2-chloroethyl ethyl sulfide (CEES) has long been a research focus in chemical protection and environmental remediation.[1,2] The decontamination mechanisms of HD and CEES mainly include physical adsorption,[3] dehydrochlorination,[4] oxidation,[5,6] and hydrolysis.[7] Catalytic decontamination materials developed based on these mechanisms include hypochlorites,[8] zeolites,[7] metal oxides,[6] metal–organic frameworks (MOFs),[9–11] and polyoxometalates(POMs).[12–16] Among these, physical adsorption is prone to cause secondary pollution from the adsorbent;[10] dehydrochlorination generally shows low kinetic efficiency for HD/CEES decontamination;[17] oxidation carries the risk of over-oxidation (possibly generating more toxic sulfone products),[18] and some systems rely on harsh conditions such as light irradiation. In contrast to the above three pathways, hydrolysis yields less toxic products but is constrained by the poor water solubility of HD and its simulants; additionally, the formation of intermediates impedes the further progress of the reaction, thus limiting its practical application.[2]

Compared with traditional catalytic decontamination materials (hypochlorites, zeolites, metal oxides), POMs possess dual-functional characteristics (acidic sites and redox-active sites) and core advantages of tunable structure (performance optimization *via* transition metal doping or organic functional group modification), making them widely applicable in all four decontamination mechanisms. In recent years, an increasing number of novel and efficient POM catalysts have been used for HD/CEES decontamination.[12–16]

Currently, in POM-based HD/CEES decontamination involving solvents, the extensive use of organic solvents is a prominent feature of mainstream schemes.[4] The core consideration is to improve substrate solubility, which is premised on the low solubility of POMs in organic solvents. Especially at low POM amount, the insufficient exposure of active sites cannot be alleviated by the good solubility of the substrate; moreover, this scheme fails to consider the potential secondary pollution risk of organic solvents, which constitutes a major limitation for technical application.

To overcome the inherent defects of the above organic solvent systems, this study selected water as the green solvent and H_2O_2 as the green oxidant, and specifically adopted Keplerate-type POMs as the catalytic core. Due to their unique cage-like topology, Keplerate-type POMs have a large specific surface area, high active site density, and sufficient site exposure. Their abundant coordination sites and tunable charge properties not only adapt to the aqueous reaction environment to alleviate the poor solubility of traditional POMs but also

[a]*State Key Laboratory of Chemical Resource Engineering, College of Chemistry, Beijing University of Chemical Technology, Beijing, 100029, China. E-mail: zhouys@mail.buct.edu.com*

[b]*School of Environment and Health, Yanching Institute of Technology, Langfang 065201, China*

exhibit excellent catalytic selectivity and stability in thioether oxidation reactions.[12,19,20]

Based on this, two Keplerate-type nano-polyoxometalates were selected as research objects: $(NH_4)_{42}[Mo^{VI}_{72}Mo^{V}_{60}O_{372}(CH_3COO)_{30}(H_2O)_{72}]\cdot ca.300H_2O\cdot ca.10CH_3COONH_4$ (denoted as $\{Mo_{132}\text{-}Ac^-\}$)[21] and $(NH_4)_{72-n}[(H_2O)_{81-n}{}^{+}(NH_4)_n \subset \{(Mo^{VI})Mo^{VI}_5O_{21}(H_2O)_6\}_{12}\{Mo^{V}_2O_4(SO_4)_{30}\}]\cdot ca.200H_2O$ (denoted as $\{Mo_{132}\text{-}SO_4{}^{2-}\}$).[22] The difference between the two lies in the ligands on the anionic $\{Mo_2\}$ units: the anions of $\{Mo_{132}\text{-}Ac^-\}$ and $\{Mo_{132}\text{-}SO_4{}^{2-}\}$ carry 42 and 72 negative charges, respectively (Fig. 1). Using water as the solvent and H_2O_2 as the oxidant, the decontamination conditions were optimized *via* the single-factor method. The catalytic decontamination performance, reaction kinetics, and decontamination mechanism of the two catalysts for CEES were investigated.

2 Experimental

2.1 Reagents and instruments

CH_3COOH (analytical grade), $N_2H_4\cdot H_2SO_4$ (analytical grade), $(NH_4)_6Mo_7O_{24}\cdot 4H_2O$ (analytical grade), CH_3COONH_4 (analytical grade), CEES (analytical grade), dichloromethane (analytical grade), thymolphthalein (analytical grade), 1,3-dichlorobenzene (chromatographic grade), ethanol (analytical grade), NaOH (analytical grade). All chemicals were purchased directly and used without further purification.

Fourier transform infrared (FT-IR) spectrometer (ICAN9 model): tested in the range of 4000–400 cm^{-1} by KBr pellet method (for catalyst characterization). UV-visible (UV-vis) spectrophotometer (for aqueous phase absorbance determination). GC-FID (GC-5890): equipped with a Kb-5 column (30 m × 320 μm × 0.25 μm); column temperature: 120 °C, inlet temperature: 220 °C, detector temperature: 250 °C (for qualitative and quantitative analysis of reaction materials). X-ray photoelectron spectrometer (XPS, Axis Supra). Magnetic stirrer (TH70-85-2). Reactor: glass screw-cap sample vial (3 mL, 16 × 35 mm).

2.2 Catalyst preparation

$\{Mo_{132}\text{-}Ac^-\}$[21] and $\{Mo_{132}\text{-}SO_4{}^{2-}\}$[22] were synthesized according to the literature and characterized by FT-IR and XPS.

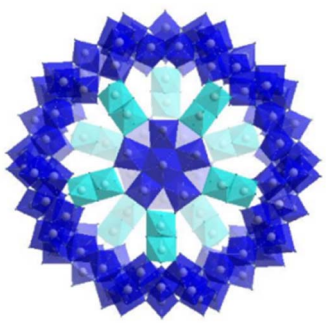

Fig. 1 The capsular structure of nano-polyoxometalate cluster $\{Mo_{132}\}$ (color code: Mo^{VI}, blue and Mo^{V}, cyan).

2.3 Decontamination of CEES

In 500 μL deionized water, 5 μL CEES (0.042 mmol) and a preset amount of catalyst $\{Mo_{132}\text{-}L\}$ ($L = Ac^-$, $SO_4{}^{2-}$) were added, followed by H_2O_2 (30%) to initiate the reaction. After reaction at room temperature for a designated time, 500 μL of dichloromethane and 2.4 μL of 1,3-dichlorobenzene (21 μmol) as the internal standard were added. The mixture was stirred for 10 min to facilitate extraction, followed by standing for phase separation. The aqueous layer was carefully withdrawn using a pipette, and quantitative analysis of the product was performed by gas chromatography (GC) employing the internal standard method.

2.4 Catalyst reusability

0.77 μmol of catalyst $\{Mo_{132}\text{-}L\}$ ($L = Ac^-$, $SO_4{}^{2-}$) was used for the reusability test. After each reaction cycle, the catalyst was recovered by concentration, dried at 60 °C, and reused for the next catalytic run.

3 Results and discussion

3.1 Characterization

$\{Mo_{132}\text{-}Ac^-\}$ and $\{Mo_{132}\text{-}SO_4{}^{2-}\}$ were synthesized strictly following the protocols reported in the literature,[21,22] and characterized by FT-IR, PXRD and XPS. Notably, their FT-IR spectra (including characteristic peak positions and intensities) and XPS results (*e.g.*, Mo valence state distribution) were in full accord with those documented in the aforementioned references, confirming the successful reproduction of the target catalysts as reported.[21,22]

The PXRD patterns of $\{Mo_{132}\text{-}Ac^-\}$ and $\{Mo_{132}\text{-}SO_4{}^{2-}\}$ (Fig. S1) exhibit characteristic low-angle peaks ($2\theta \approx 8°$, 11°) consistent with $\{Mo_{132}\}$-type Keplerate clusters. No impurity peaks are observed, confirming the high phase purity and good crystallinity of the samples, which is in line with literature reports and verifies the successful synthesis.[21,22]

3.2 CEES decontamination performance of catalysts

3.2.1 Effect of the amount of catalyst. 5 μL CEES (0.042 mmol), 6 μL H_2O_2 (30%, 0.059 mmol), and different amount of $\{Mo_{132}\text{-}Ac^-\}$ (0, 5, 10, 20, 30 mg) were added to 500 μL H_2O, and the reaction was conducted at room temperature for 10 min. Results showed that CEES was barely degraded without the catalyst, indicating that H_2O_2 alone cannot effectively decontaminate CEES. When the catalyst amount increased from 5 mg to 10 mg, the conversion rate increased from 95.46% to 98.84% (Fig. 2(b)), with a small amount of highly toxic $CEESO_2$ detected alongside the target product CEESO (Fig. 2(a)). Decontamination products were qualitatively identified by comparison with standard substances. The GC-FID chromatograms of CEES, internal standard (1,3-dichlorobenzene), CEESO, and $CEESO_2$ standards are shown in Fig. S2. GC-FID quantification was performed by the internal standard method with 1,3-dichlorobenzene. Response factors of CEES, CEESO, and $CEESO_2$. The internal standard were calibrated for quantitative accuracy. No

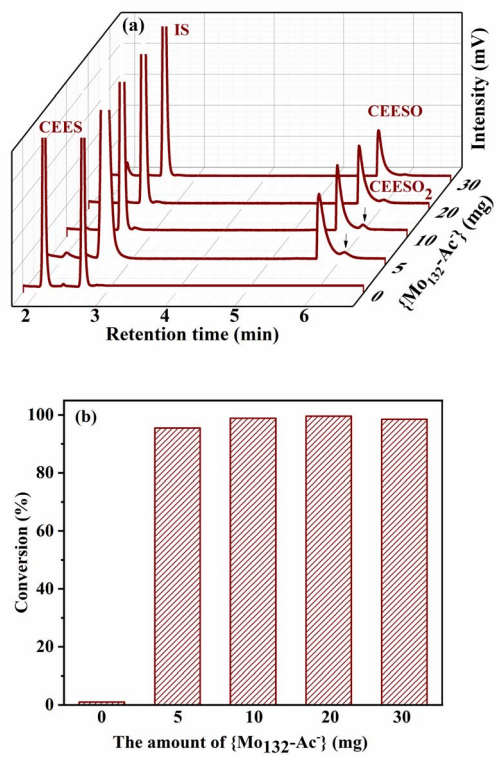

Fig. 2 (a) GC-FID signals show the effects of the amount of { Mo_{132}-Ac^-} on CEES decontamination. (b) CEES conversion rate as a function of {Mo_{132}-Ac^-} amount. Data are the average of three parallel experiments with an experimental error of ±2%.

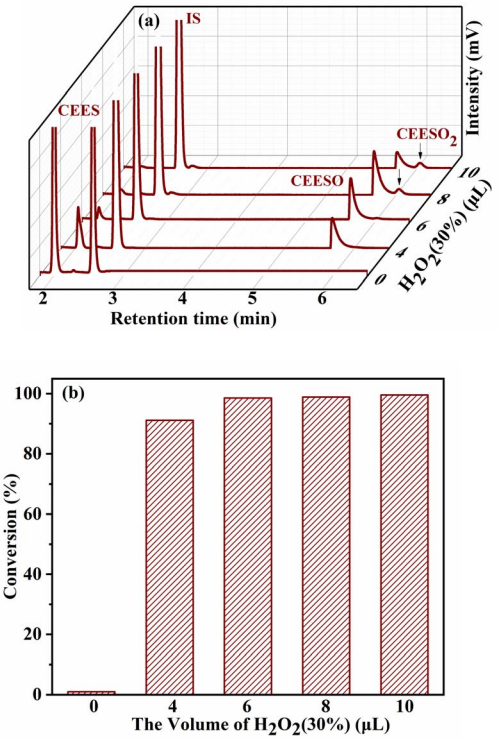

Fig. 3 (a)GC-FID chromatograms illustrating the oxidation progress of CEES with varying amounts of H_2O_2 (30%). (b) Effect of H_2O_2 (30%) volume (μL) on CEES conversion rare. Data are the average of three parallel experiments with an experimental error of ±2%.

significant interference peaks were observed, eliminating matrix effects on results.

At a catalyst amount of 20 mg, the conversion rate was 98.59%, slightly lower than that at 10 mg, but $CEESO_2$ formation was minimized. To avoid $CEESO_2$ and ensure high conversion, the catalyst amount was set to 0.77 μmol.

3.2.2 Effect of the amount of 30% H_2O_2 on CEES oxidation. 5 μL CEES (0.042 mmol), 20 mg {Mo_{132}-Ac^-} (0.77 μmol), and different amount of H_2O_2 (30%, 0, 4, 6, 8, 10 μL) were added to 500 μL H_2O, and the reaction was conducted at room temperature for 10 min. Results showed that almost no decontamination occurred without H_2O_2. With the increase of H_2O_2 amount, the conversion rate increased to 91.12% (4 μL), 98.59% (6 μL), 98.84% (8 μL), and 99.59% (10 μL) (Fig. 3(b)). When H_2O_2 amount exceeded 6 μL, $CEESO_2$ was detected alongside CEESO (Fig. 3(a)). Thus, the amount of H_2O_2 (30%) was set to 6 μL.

3.2.3 Effect of reaction time. Based on the optimized amount of catalyst and oxidant, experiments were conducted to investigate the effect of reaction time (0, 1, 3, 5, 7, 10 min) on the decontamination rate. For {Mo_{132}-Ac^-}, the conversion rate increased significantly in the first 5 min: 46.01% (1 min), 61.48% (3 min), 77.13% (5 min). After 7 min, the conversion rate plateaued, reaching 98.59% at 10 min. For {Mo_{132}-SO_4^{2-}}, the conversion trend was consistent but higher: 54.80% (1 min), 79.17% (3 min), 94.13% (5 min), 99.29% (7 min), 99.69% (10 min), with nearly complete CEES decontamination at 7 min (Fig. 4). Notably, under optimized conditions, CEESO was the dominant product at 10 min for both catalysts, indicating that product control relies on appropriate amount of catalyst and H_2O_2.

Plots of $\ln(C_t/C_0)$ (C_t: CEES concentration at time t; C_0: initial CEES concentration) *versus* time showed approximately linear relationships for both catalysts, confirming first-order reaction kinetics. The first-order kinetic constants of {Mo_{132}-Ac^-} and {Mo_{132}-SO_4^{2-}} were 0.39 ± 0.041 min^{-1} and 0.60 ± 0.046 min^{-1}, respectively (Fig. 5).

Compared with recent aqueous-phase POM-based CEES decontamination systems, {Mo_{132}-SO_4^{2-}} exhibits superior comprehensive performance. POM@CTF catalyst showed a kinetic constant of 0.061 min^{-1} and 99% selectivity,[13] while {$PMo_{11}MoCu_8$} was used for 4 cycles.[16] In contrast, {Mo_{132}-SO_4^{2-}} achieves a higher 0.60 min^{-1} kinetic constant, >99% selectivity, and >90% conversion after 5 cycles without organic solvents, highlighting the ligand regulation strategy and green aqueous system's application potential.

3.3 Decontamination mechanism

Notably, in the decontamination system, CEES was barely degraded when only the catalyst {Mo_{132}-L} or H_2O_2 was added. In contrast, the CEES conversion rate increased significantly when both were present simultaneously. Thus, CEES decontamination relies on the synergistic effect of the catalyst and

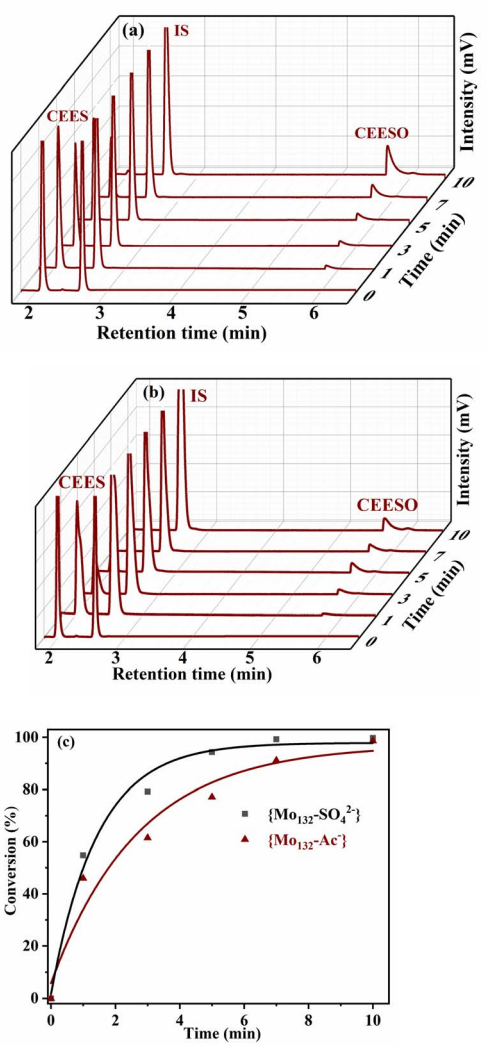

Fig. 4 GC-FID chromatograms show the time profiles for the decontamination of CEES: (a) {Mo_{132}-Ac^-}, (b) {Mo_{132}-SO_4^{2-}}. Effect of reaction time on conversion of CEES (c). Data are the average of three parallel experiments with an experimental error of ±2%.

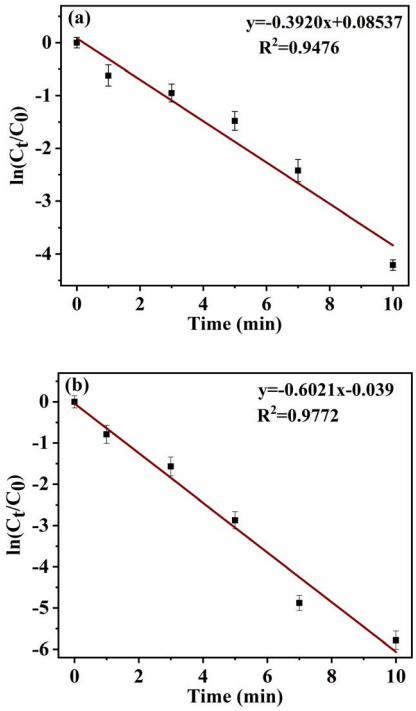

Fig. 5 Kinetic analysis of CEES oxidation catalyzed by {Mo_{132}-L} (L = Ac^-, SO_4^{2-}): (a) {Mo_{132}-Ac^-}, (b) {Mo_{132}-SO_4^{2-}}.

oxidant. Upon reaction with H_2O_2, the terminal Mo_2=O sites are converted into peroxo-molybdenum species ($Mo(O_2)$) *via* peroxo coordination, as verified by XPS. These peroxo species act as the actual active intermediates for the selective oxidation of CEES to CEESO.

In both catalysts, Mo exists in two valence states: +5 and +6. The chemical formulas with valence state labels for {Mo_{132}-Ac^-} and {Mo_{132}-SO_4^{2-}} are as follows: $(NH_4)_{42}[Mo_{72}^{VI}Mo_{60}^{V}O_{372}(CH_3COO)_{30}(H_2O)_{72}]\cdot ca.\ 300H_2O\cdot ca.\ 10CH_3COONH_4$ (note: slight discrepancy from the formula in the introduction) and $(NH_4)_{72-n}[(H_2O)_{81-n}{}^{+}(NH_4)_n \subset \{(Mo^{VI})Mo_5^{VI}O_{21}(H_2O)_6\}_{12}\{Mo_2^{V}O_4(SO_4)_{30}\}]\cdot ca.\ 200H_2O$. Their XPS characterization results are shown in Fig. 6 and S3.

As presented in Fig. 6(a), before the addition of H_2O_2, the high-resolution Mo 3d spectrum of {Mo_{132}-Ac^-} exhibited four peaks at 231.5, 232.7, 234.7, and 235.8 eV.[12] The peaks at 231.5 eV and 234.7 eV were assigned to Mo^V $3d_{5/2}$ and Mo^V $3d_{3/2}$, respectively, while those at 232.7 eV and 235.8 eV corresponded to Mo^{VI} $3d_{5/2}$ and Mo^{VI} $3d_{3/2}$, according to the reported XPS reference values for molybdenum-based compounds.[23] After adding H_2O_2 (Fig. 6(b)), the Mo 3d spectrum of {Mo_{132}-Ac^-} showed only two peaks at 232.7 eV and 235.8 eV, which were attributed to Mo^{VI} $3d_{5/2}$ and Mo^{VI} $3d_{3/2}$, indicating that Mo^V was completely oxidized to Mo^{VI} by H_2O_2.

As shown in Fig. 6(c), after the simultaneous addition of H_2O_2 and the substrate CEES to the catalyst, the high-resolution Mo 3d spectrum was restored to that before H_2O_2 addition (four peaks). The peaks at 231.5 eV and 234.9 eV were assigned to Mo^V $3d_{5/2}$ and Mo^V $3d_{3/2}$, respectively, and those at 232.8 eV and 235.9 eV corresponded to Mo^{VI} $3d_{5/2}$ and Mo^{VI} $3d_{3/2}$, in line with the reported XPS reference values for molybdenum-containing compounds.[23] These results confirm that the {Mo_{132}-Ac^-} catalyst was regenerated after the addition of H_2O_2 and CEES.

The {Mo_{132}-SO_4^{2-}} catalyst exhibited an identical trend. Prior to H_2O_2 addition, the high-resolution Mo 3d XPS spectrum of {Mo_{132}-SO_4^{2-}} (Fig. S3a) displayed four characteristic peaks at 231.5, 232.9, 234.9, and 235.9 eV. The peaks at 231.5 eV (Mo^V $3d_{5/2}$) and 234.9 eV (Mo^V $3d_{3/2}$) are indicative of Mo^V species, while those at 232.9 eV (Mo^{VI} $3d_{5/2}$) and 235.9 eV (Mo^{VI} $3d_{3/2}$) correspond to Mo^{VI}. Upon H_2O_2 introduction (Fig. S3b), only two peaks at 232.6 eV and 235.8 eV were observed in the Mo 3d spectrum of {Mo_{132}-SO_4^{2-}}, which can be ascribed to Mo^{VI} $3d_{5/2}$ and Mo^{VI} $3d_{3/2}$, confirming the complete oxidation of Mo^V to Mo^{VI} by H_2O_2.

Following the co-addition of H_2O_2 and substrate CEES to the catalyst (Fig. S3c), the high-resolution Mo 3d spectrum of

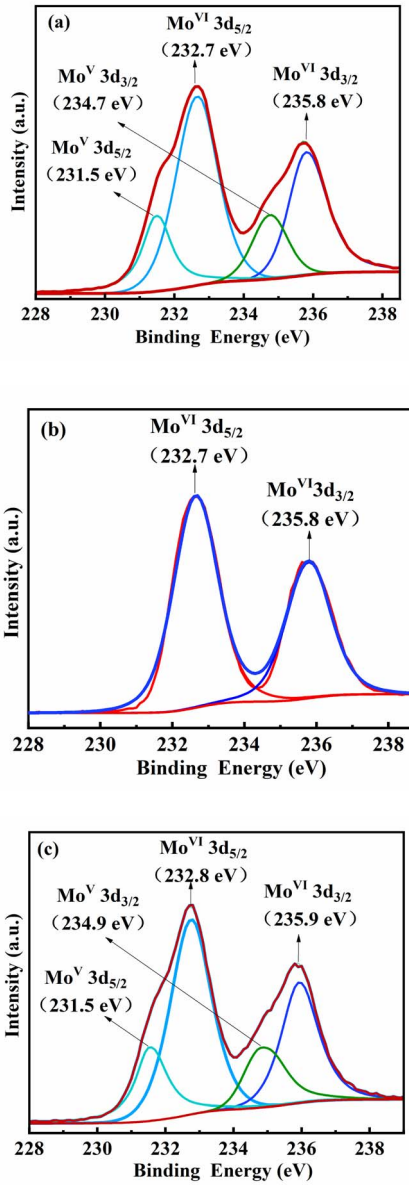

Fig. 6 XPS of Mo 3d of {Mo_{132}-Ac^-} (a), Mo 3d of {Mo_{132}-Ac^-} after adding H_2O_2 (b), Mo 3d of {Mo_{132}-Ac^-} after adding H_2O_2 and substrate CEES (c).

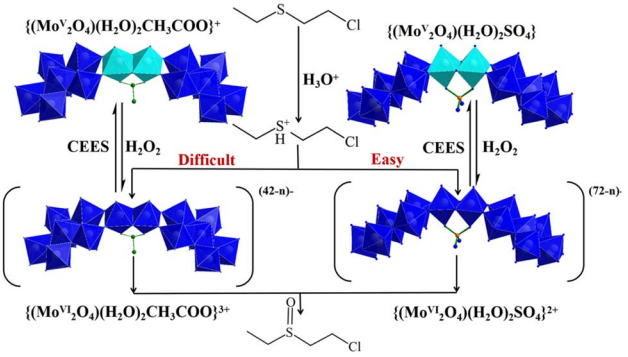

Fig. 7 Comparison of the difficulty of selective oxidation of CEES with {Mo_{132}-L} (L = Ac^-, SO_4^{2-}) (color code: Mo^{VI}, blue and Mo^V, cyan).

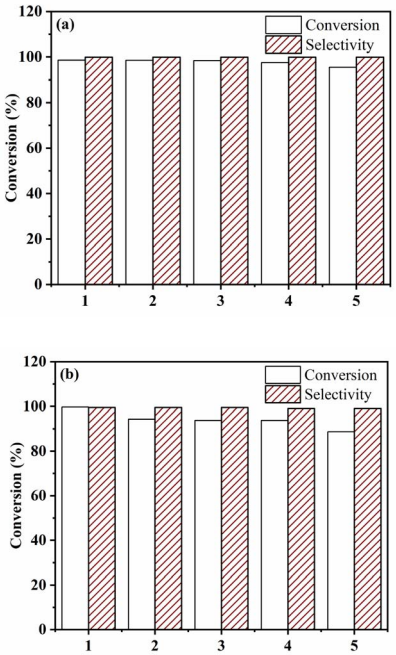

Fig. 8 Influence of catalyst cycle times on conversion and selectivity: (a) {Mo_{132}-Ac^-}, (b) {Mo_{132}-SO_4^{2-}}. Data are the average of three parallel experiments with an experimental error of ±2%.

{Mo_{132}-SO_4^{2-}} was recovered to its state prior to H_2O_2 addition, exhibiting four peaks at 231.5, 232.9, 234.8, and 236.0 eV. These peaks are assigned to Mo^V ($3d_{5/2}$: 231.5 eV; $3d_{3/2}$: 234.8 eV) and Mo^{VI} ($3d_{5/2}$: 232.9 eV; $3d_{3/2}$: 236.0 eV), consistent with the initial spectral profile. These findings verify the regeneration of the {Mo_{132}-SO_4^{2-}} catalyst after the combined treatment with H_2O_2 and CEES.[12]

The negative charges of {Mo_{132}-Ac^-} (42^-) and {Mo_{132}-SO_4^{2-}} (72^-) have been confirmed by elemental analysis and charge balance calculations.[21,22] For the {Mo_{132}-Ac^-}, the pH of the reaction solution was kept at 4.6–4.8 before and after the addition of H_2O_2. Similarly, for the {Mo_{132}-SO_4^{2-}}, the reaction pH was also maintained at 3.5–3.7 throughout the process. Notably, the Keplerate {Mo_{132}} clusters possess a well-defined porous spherical structure with pore openings of *ca.* 9 Å, which allow the entry of CEES molecules into the clusters. However, only the terminal Mo=O groups exposed on the outer spherical surface are accessible to H_2O_2 and responsible for the formation of peroxo-molybdenum species ($Mo(O_2)$). Consequently, the catalytic oxidation of CEES to CEESO proceeds exclusively on the outer surface of {Mo_{132}}. In the acidic aqueous system, the sulfur atom in CEES is prone to protonation to form the R–S^+(H)–R′ intermediate. Compared with {Mo_{132}-Ac^-}, {Mo_{132}-SO_4^{2-}} with more negative charges exhibits stronger electrostatic interactions with the positively charged R–S^+(H)–R′, bringing the substrate closer to the catalyst surface. Peroxo-molybdenum species ($Mo(O_2)$) are formed from the reaction of the 132 terminal Mo=O groups on {Mo_{132}} with

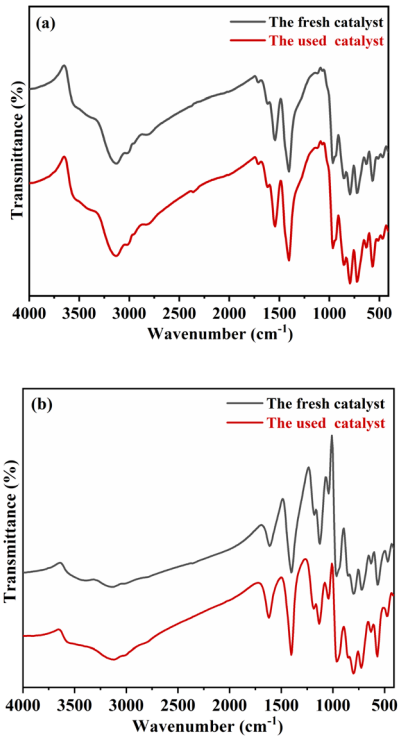

Fig. 9 IR spectra of the fresh and recovered catalysts after catalysis reaction: (a) {Mo_{132}-Ac^-}, (b) {Mo_{132}-SO_4^{2-}}.

H_2O_2. All these Mo=O oxygen atoms lie on the outer spherical surface, while the *trans*-positioned H_2O ligands of the 72 Mo^{VI} centers point toward the center of the sphere. These peroxo intermediates then efficiently oxidize CEES to CEESO. This inference is fully consistent with the catalytic performance data of the two catalysts: {Mo_{132}-SO_4^{2-}} shows a higher kinetic constant (0.60 ± 0.046 min^{-1} *vs.* 0.39 ± 0.041 min^{-1} for {Mo_{132}-Ac^-}) and a faster reaction rate (nearly complete conversion within 7 min), highlighting the catalytic advantage brought by ligand-regulated charge properties,[24] as shown in Fig. 7.

3.4 Catalyst reusability

Reusability tests showed that after 5 cycles, {Mo_{132}-Ac^-} and {Mo_{132}-SO_4^{2-}} maintained a CEES conversion rate >90% and selectivity >99% (Fig. 8). FT-IR spectra of the recovered catalysts showed no significant changes compared with fresh catalysts (Fig. 9), indicating good stability of {Mo_{132}-Ac^-} (or {Mo_{132}-SO_4^{2-}}) under reaction conditions. Meanwhile, XPS spectra confirmed that the catalysts were regenerated after CEES catalytic decontamination (Fig. 6 and S3).

4 Conclusions

Keplerate-type {Mo_{132}} polyoxometalates with different ligands (Ac^- and SO_4^{2-}) were successfully applied for CEES decontamination in green aqueous phase using H_2O_2 as oxidant. The ligand effect was systematically investigated: {Mo_{132}-SO_4^{2-}} with more negative charges exhibits a higher first-order kinetic constant (0.60 min^{-1}) and CEES conversion (99.69%) than {Mo_{132}-Ac^-}, attributed to the enhanced electrostatic interaction between catalyst and CEES. By optimizing the catalyst and H_2O_2 dosage, CEES is selectively oxidized to low-toxic CEESO with selectivity >99%. Both catalysts maintain excellent activity (>90% conversion) and selectivity (>99%) after 5 cycles, supported by FT-IR and XPS, which confirms structural stability. This work provides a new strategy for regulating catalytic performance *via* ligand engineering of Keplerate-type POMs and offers a practical, green solution for rapid detoxification of mustard gas simulants.

Notably, this work focuses on the decontamination of pure CEES in aqueous media; future studies could explore the catalytic performance in complex matrices (*e.g.*, soil extracts or wastewater) to further validate practical applicability. Additionally, the ligand regulation strategy reported herein provides a general approach for designing high-performance POM-based catalysts for thioether oxidation reactions.

Author contributions

Jianbo Yin: investigation, writing – original draft, review & editing, methodology, formal analysis, data curation. Liming Sun: formal analysis, data curation. Yunshan Zhou: conceptualization, methodology, resources, writing – review & editing, supervision, project administration, funding acquisition. Lijuan Zhang: writing – review & editing, supervision.

Conflicts of interest

The authors declare that they have no known competing financial interests or personal relationships that could have appeared to influence the work reported in this paper.

Data availability

The data supporting the findings of this study are available within the article and its supplementary information (SI). The SI contains detailed procedures for the synthesis of {Mo_{132}-Ac^-} and {Mo_{132}-SO_4^{2-}} catalysts, GC-FID spectra of CEES, CEESO, $CEESO_2$ and the internal standard (1,3-dichlorobenzene) for quantitative analysis (Fig. S2), and full XPS Mo 3d characterization data of {Mo_{132}-SO_4^{2-}} (Fig. S3). All other relevant data are available from the corresponding author upon reasonable request. Supplementary information is available. See DOI: https://doi.org/10.1039/d6ra00608f.

Acknowledgements

The financial support from the National Natural Science Foundation of China (No. 21976013) is acknowledged.

Notes and references

1 K. Kim, O. G. Tsay, D. A. Atwood and D. G. Churchill, Destruction and detection of chemical warfare agents, *Chem. Rev.*, 2011, **111**, 5345–5403.

2 Y. C. Yang, J. A. Baker and J. R. Ward, Decontamination of chemical warfare agents, *Chem. Rev.*, 1992, **92**, 1729–1743.
3 Y. H. Cheung, K. K. Ma, L. H. Van, X. Liu, M. C. Wasson, X. J. Wang, K. B. Idrees, W. Gong, R. Cao, J. J. Mahle, T. Islamoglu, G. W. Peterson, K. M. De, J. H. Xin and O. K. Farha, Immobilized regenerable active chlorine within a zirconium-based MOF textile composite to eliminate biological and chemical threats, *J. Am. Chem. Soc.*, 2021, **143**, 16777–16785.
4 J. Dong, D. Zhang, P. X. Zhang, P. C. Liu, J. Li, J. Bai, Y. N. Chi and C. W. Hu, Polyoxometalates for the decontamination of chemical warfare agents: From structure and composition regulation to performance enhancement, *Coord. Chem. Rev.*, 2024, **517**, 215998.
5 C. R. Ringenbach, S. R. Livingston, D. Kumar and C. C. Landry, Vanadium-doped acid-prepared mesoporous silica: synthesis, characterization, and catalytic studies on the oxidation of a mustard gas analogue, *Chem. Mater.*, 2005, **17**, 5580–5586.
6 Y. T. Guo, L. C. Kong, M. L. Lei, Y. Xin, Y. J. Zuo and W. M. Chen, Effect of crystallographic structure of MnO_2 on decontamination of 2-CEES, *J. Mol. Liq.*, 2021, **333**, 115946.
7 Y. R. Son, M. K. Kim, S. G. Ryu and H. S. Kim, Rapid capture and hydrolysis of a sulfur mustard gas in silver-ion-exchanged zeolite Y, *ACS Appl. Mater. Interfaces*, 2018, **10**, 40651–40660.
8 M. Labaška, M. Gál, T. Mackuak, J. Švorec, J. Kučera, J. Helenin, V. Svitková and J. Ryba, Neutralizing the threat: A comprehensive review of chemical warfare agent decontamination strategies, *J. Environ. Chem. Eng.*, 2024, **12**, 114243.
9 Y. R. Son, S. G. Ryu and H. S. Kim, Rapid adsorption and removal of sulfur mustard with zeolitic imidazolate frameworks ZIF-8 and ZIF-67, *Microporous Mesoporous Mater.*, 2020, **293**, 109819–109827.
10 M. E. López, C. Montoro, A. L. Rodríguez, S. D. Cervantes, P. A. Lozano, J. L. Cenís, E. Barea and J. A. Navarro, Textile/metal-organic-framework composites as self-detoxifying filters for chemical-warfare agents, *Angew. Chem., Int. Ed.*, 2015, **127**, 6894–6898.
11 X. Hu, Y. Yang, N. Li, C. C. Huang, Y. S. Zhou, L. J. Zhang, Y. X. Zhong, P. J. Wang and Y. F. Chen, Multi-pathway and multiple-mechanism in action together: High-efficient visible-light photocatalytic oxidation and hydrolysis of CEES by a ligand-differentiated Zr-MOF, *Sep. Purif. Technol.*, 2025, **362**, 131794.
12 J. B. Yin, C. C. Huang, Y. S. Zhou, L. J. Zhang, N. Li and R. Sun, Selective oxidation of 2-chloroethyl ethyl sulfide in aqueous media catalyzed by $\{Mo_{72}M_{30}\}$ nano-polyoxometalate clusters differentiating the catalytic activity of nodal metals, *Ind. Eng. Chem. Res.*, 2022, **61**, 7699–7708.
13 Q. S. Zhu, H. Y. An, T. Q. Xu, Y. H. Chen, Y. T. Wei and H. Sun, Polyoxometalates embedded into covalent triazine frameworks regulating charge transfer for visible-light-driven synthesis of functionalized sulfoxides and detoxification of mustard gas simulants, *ACS Sustain. Chem. Eng.*, 2024, **12**, 1655–1665.
14 Y. Yang, F. S. Tao, L. J. Zhang, Y. S. Zhou, Y. X. Zhong, S. B. Tian and Y. A. Wang, Preparation of a porphyrin-polyoxometalate hybrid and its photocatalytic decontamination performance for mustard gas simulant 2-chloroethyl ethyl sulfide, *Chin. Chem. Lett.*, 2022, **33**, 2625–2629.
15 K. H. Ji, Y. N. Liu, Y. H. Luo, X. Zhang, Y. F. Bai, H. L. Yue, P. T. Ma, J. Y. Niu and J. P. Wang, Metalloligand hybrid polyoxometalates for efficient selective photocatalytic oxidation of sulfides to sulfoxides under visible light irradiation, *J. Phys. Chem. C*, 2023, **127**, 256–264.
16 X. Y. Ji, M. Xing, M. C. Zhu, X. Bai, Y. L. Yang, A. G. Zhang, Y. Lu and S. X. Liu, Rapid oxidative detoxification of mustard simulant by the multisite synergistic catalytic action of $\{PMo^{VI}_{11}Mo^{V}O_{40}Cu^{I}_{8}\}$ Units, *Inorg. Chem.*, 2024, **63**, 346–352.
17 M. Florent, D. A. Giannakoudakis and T. J. Bandosz, Mustard gas surrogate interactions with modified porous carbon fabrics: effect of oxidative treatment, *Langmuir*, 2017, **33**, 11475–11483.
18 M. Y. Yu, J. H. Liu, F. W. Liu, F. Zou, L. Zhang, Q. P. Gao, X. Y. Ren, Q. Zhang, S. Z. Liu, C. P. Dong, T. T. Guo, F. Ma and W. Y. Pei, Polyoxometalate-Incorporated Cu^{I}-Resorcin [4]arene Metal Organic Complexes as Heterogeneous Catalysts for Catalytic Oxidation of Mustard Gas Simulant, *Eur. J. Inorg. Chem.*, 2023, **26**, e202300221.
19 A. Rezaeifard, R. Haddad, M. Jafarpour and M. Hakimi, Catalytic epoxidation activity of keplerate polyoxomolybdate nanoball toward aqueous suspension of olefins under mild aerobic conditions, *J. Am. Chem. Soc.*, 2013, **135**, 10036–10039.
20 P. Wang, T. Wang, M. Xu, Z. Gao, H. Y. Li, B. W. Li and Y. Q. Wang, Keplerate polyoxomolybdate nanoball mediated controllable preparation of metal-doped molybdenum disulfide for electrocatalytic hydrogen evolution in acidic and alkaline media, *Chin. Chem. Lett.*, 2023, **34**, 108930.
21 A. Müller, E. Krickemeyer, H. Bögge, M. Schmidtmann and F. Peters, Organizational forms of matter: an inorganic super fullerene and keplerate based on molybdenum oxide, *Angew. Chem., Int. Ed.*, 1998, **37**, 3359–3363.
22 A. Müller, E. Krickemeyer, H. Bögge, B. B. Schmidtmann and M. O. Talismanova, Drawing small cations into highly charged porous nanocontainers reveals “water” assembly and related interaction problems, *Angew. Chem., Int. Ed.*, 2003, **42**, 2085–2090.
23 X. Xu, B. L. Luo, L. L. Wang, L. Xu and L. XU, An unprecedented nanocage-like and heterometallic $[Mo_3^{IV}O_4]$- polyoxomolybdate hybrid, *Dalton Trans.*, 2018, **47**(10), 3218–3222.
24 D. M. Chevrier, L. Raich, C. Rovira, A. Das, Z. Z. Luo, Q. F. Yao, A. Chatt, J. P. Xie, R. C. Jin, J. Akola and P. Zhang, Molecular-scale ligand effects in small gold-thiolate nanoclusters, *J. Am. Chem. Soc.*, 2018, **140**, 15430–15436.